

Octahedral deformations and cationic displacements in the ferroelectric $\text{PbHf}_{0.8}\text{Ti}_{0.2}\text{O}_3$: a neutron powder diffraction study from 10 to 770 K

Ch. Muller,^{a*} J.-L. Baudour,^a C. Bedoya,^b F. Bouree,^c J.-L. Soubeyrou^d and M. Roubin^b

^aLaboratoire des Matériaux Multiphasés et Interfaces, Université de Toulon et du Var, BP 132, 83957 La Garde CEDEX, France,

^bLaboratoire des Matériaux à Finalités Spécifiques, Université de Toulon et du Var, BP 132, 83957 La Garde CEDEX, France, ^cLaboratoire Léon Brillouin, CE-Saclay, 91191 Gif-sur-Yvette, France, and ^dLaboratoire de Cristallographie—CNRS and Institut Laue—Langevin, BP 166, 38042 Grenoble CEDEX 09, France

Correspondence e-mail: muller@univ-tln.fr

Neutron powder diffraction data, collected over the temperature range 10–770 K, have been analysed in order to make a detailed characterization of the sequence of phase transitions occurring in the Hf-rich ferroelectric $\text{PbHf}_{0.8}\text{Ti}_{0.2}\text{O}_3$, titanium hafnium lead oxide. Over the whole temperature range this compound undergoes two phase transitions, which involve cationic displacements and octahedral deformations (tilt and/or distortion) leading to strongly distorted perovskite-type structures. The first transition appears around 415 K between two ferroelectric rhombohedral phases: a low-temperature nonzero-tilt phase F_{RL} (space group $R3c$) and an intermediate zero-tilt phase F_{RH} (space group $R3m$). The second one, detected around 520 K, is associated with a ferroelectric to-paraelectric transition between the F_{RH} phase and the P_C cubic phase (space group $Pm\bar{3}m$). From high-resolution neutron powder diffraction data (diffractometer 3T2-LLB, Saclay, France, $\lambda = 1.2251 \text{ \AA}$), the crystallographic structure of the three successive phases has been accurately determined at the following temperatures: $T = 10 \text{ K}$ (F_{RL}): space group $R3c$, $Z = 6$, $a_{\text{hex}} = 5.7827(1)$, $c_{\text{hex}} = 14.2702(4) \text{ \AA}$, $V_{\text{hex}} = 413.26(2) \text{ \AA}^3$; $T = 150 \text{ K}$ (F_{RL}): space group $R3c$, $Z = 6$, $a_{\text{hex}} = 5.7871(1)$, $c_{\text{hex}} = 14.2735(4) \text{ \AA}$, $V_{\text{hex}} = 413.98(3) \text{ \AA}^3$; $T = 290 \text{ K}$ (F_{RL}): space group $R3c$, $Z = 6$, $a_{\text{hex}} = 5.7943(1)$, $c_{\text{hex}} = 14.2742(5) \text{ \AA}$, $V_{\text{hex}} = 415.04(3) \text{ \AA}^3$; $T = 440 \text{ K}$ (F_{RH}): space group $R3c$, $Z = 6$, $a_{\text{hex}} = 5.8025(1)$, $c_{\text{hex}} = 14.2648(4) \text{ \AA}$, $V_{\text{hex}} = 415.94(3) \text{ \AA}^3$; $T = 520 \text{ K}$ (P_C): space group $Pm\bar{3}m$, $Z = 1$, $a_{\text{cub}} = 4.1072(2) \text{ \AA}$, $V_{\text{cub}} = 69.29(1) \text{ \AA}^3$. In addition, a neutron powder thermodiffraction experiment, performed between 290 and 770 K (diffractometer D1B-ILL, Grenoble, France, $\lambda = 2.533 \text{ \AA}$), has been used to study *in situ* the temperature-induced phase transitions. From sequential Rietveld refinements, the temperature dependence of the cation displacements and the rotation and/or distortion of oxygen octahedra was derived.

Received 18 May 1999

Accepted 6 September 1999

1. Introduction

The series denoted PHT and formulated as $\text{PbHf}_{1-x}\text{Ti}_x\text{O}_3$ derives from the PZT family, which is well known for its attractive ferroelectric and piezoelectric properties. As in the PZT binary phase diagram (Jaffe *et al.*, 1971; Viehland, 1995), the isomorphous solid solution PbTiO_3 – PbHfO_3 (Jaffe *et al.*, 1955) shows a large variety of phase transitions involving cationic shifts and oxygen octahedra deformations (rotation and/or distortion), leading to strongly distorted perovskite-type structures. Particularly, the Zr-rich $\text{PbZr}_{1-x}\text{Ti}_x\text{O}_3$ compounds, for x in the range 0.05–0.47, crystallize at room temperature in rhombohedral symmetry structures noted as F_{RL} and F_{RH} (Jaffe *et al.*, 1971; Ito *et al.*, 1983; Viehland, 1995).

The $F_{RL} \rightarrow F_{RH}$ phase transition can be induced either by increasing the Ti content at fixed temperature (Corker, Glazer, Whatmore *et al.*, 1998) or by increasing the temperature for a determined composition.

We report in this paper a detailed characterization of the temperature-induced phase transitions occurring in an Hf-rich PHT, *i.e.* $\text{PbHf}_{0.8}\text{Ti}_{0.2}\text{O}_3$. Indeed, this compound undergoes two phase transitions: the first occurs around 415 K between the two ferroelectric rhombohedral phases, F_{RL} and F_{RH} , and the second one, detected around 520 K, separates the phase F_{RH} from the paraelectric cubic phase P_C .

The most convenient crystallographic description of the rhombohedral phase F_{RL} , space group $R3c$ (No. 161), is that in a hexagonal unit cell with $a_{\text{hex}} \simeq 5.78$ and $c_{\text{hex}} \simeq 14.27$ Å, corresponding to a doubled 'pseudo-cubic' unit cell (Megaw & Darlington, 1975; Glazer *et al.*, 1978). This structure is defined in terms of rotation of the oxygen octahedra about the triad axis and expansion or contraction of the oxygen triangles neighbouring the shifted $\text{Hf}^{4+}/\text{Ti}^{4+}$ cations (Glazer *et al.*, 1978; Ito *et al.*, 1983; Noheda *et al.*, 1996; Cereceda *et al.*, 1997). In the intermediate phase F_{RH} , space group $R3m$ (No. 160), the tilt of the oxygen octahedra vanishes, leading to a non-doubled unit cell along the hexagonal axis, *i.e.* $a_{\text{hex}} \simeq 5.80$ and $c_{\text{hex}} \simeq 7.13$ Å, whereas cation shifts and triangle distortions subsist until the ferroelectric to-paraelectric phase transition. Above the Curie temperature T_C , the compound crystallizes in a paraelectric cubic perovskite-type structure P_C , space group $Pm\bar{3}m$ (No. 221), with a cell edge of ~ 4.10 Å. In this centrosymmetric structure, there are no cationic shifts and no octahedral distortions.

The purpose of this work is:

to accurately determine the structures of the phases F_{RL} , F_{RH} and P_C from high-resolution neutron powder diffraction data collected at 10, 150, 290, 440 and 520 K;

to follow the temperature dependence of the oxygen octahedra deformations and cation shifts through the sequence of phase transitions from a sequential analysis of the neutron powder thermodiffraction data recorded over the temperature range 290–770 K;

to link the observed structural changes to the evolution of the electrical properties.

2. Experimental

2.1. Sample synthesis

The powdered sample was synthesized using a 'Chimie Douce' process (Favotto *et al.*, 1996). An aqueous solution of lead nitrate $\text{Pb}(\text{NO}_3)_2$ was introduced into a mixture of hafnium oxalic acid $\text{H}_2[\text{HfO}(\text{C}_2\text{O}_4)_2] \cdot 5\text{H}_2\text{O}$ and titanium oxalic ammoniac acid $(\text{NH}_4)_2[\text{TiO}(\text{C}_2\text{O}_4)_2] \cdot 2\text{H}_2\text{O}$, respecting the molar ratio $\text{Hf}/\text{Ti} = 4$. The formed complex $\text{Pb}[\text{Hf}_{0.8}\text{Ti}_{0.2}\text{O}(\text{C}_2\text{O}_4)_2] \cdot y\text{H}_2\text{O}$ was dried at 333 K. The resulting gel was finally annealed in an alumina crucible at 1273 K for 3 h under a PbO atmosphere to prevent HfO_2 formation.

The chemical composition was analysed by energy-dispersive spectroscopy (EDS) coupled to a transmission electron

microscope. The analyses performed on several particles led to an Hf chemical occupancy of 0.80 ± 0.02 .

2.2. Data collection

High-resolution neutron powder diffraction patterns were recorded on the 3T2 diffractometer at the Orphée reactor at the Laboratoire Léon Brillouin (Saclay, France) with an incident wavelength of 1.2251 Å. The powdered sample was placed in a vanadium cylinder either in a helium gas flow cryostat (data collected at 10 and 150 K) or in a furnace (data collected at 440 and 520 K). Another diagram was also registered at 290 K without a sample environment. The intensities were measured by a bank of 20 ^3He cells. Full experimental details are summarized in Table 1.

Neutron powder thermodiffraction data were collected on the high-flux D1B diffractometer (Institut Laue–Langevin, Grenoble, France) equipped with a fixed-position-sensitive detector (PSD) formed by a bank of 400 ^3He cells. The powder, in a vanadium can, was heated in a furnace under vacuum from 290 to 770 K with a heating rate of 20 K h⁻¹. Diffraction patterns were registered in the angular domain 30.02–109.82° (2θ) in steps of 0.2°, with an incident wavelength of 2.533 Å. Experimental details are given in Table 2.¹

2.3. Fitting procedure

Full-profile fitting refinements of the high-resolution powder diffraction patterns were performed using the program *Fullprof* (Rodríguez-Carvajal, 1990) based on the Rietveld method. The experimental profiles were modelled using a pseudo-Voigt profile shape function ($\eta \simeq 0.2$) and the instrumental broadening was described from the Caglioti function (Caglioti *et al.*, 1958), with three refinable parameters U , V and W . Systematic error corrections (zero-point shift and asymmetry) were applied; the background was adjusted from a polynomial function and the intensities were corrected for the effects of the sample absorption ($\mu R = 0.15$). The following coherent scattering lengths were used: $b_{\text{Pb}} = 0.940 \times 10^{-12}$, $b_{\text{Hf}} = 0.780 \times 10^{-12}$, $b_{\text{Ti}} = -0.344 \times 10^{-12}$ and $b_{\text{O}} = 0.580 \times 10^{-12}$ cm.

Taking into account the small amount of an additional phase identified as being HfO_2 , monoclinic space group $P2_1/c$ (No. 14), $Z = 4$, a second set of reflections has been included in the refinement. Using the structural model of HfO_2 (Wang *et al.*, 1992) a quantitative analysis of the two phases has been performed. The profile parameters were the same as those describing the main phase, except for W which was refined independently since the observed profiles were slightly broadened owing to the small size particles of HfO_2 .

For neutron powder thermodiffraction data, full profile adjustments have been carried out using the program *Fullprof* (Rodríguez-Carvajal, 1990). Two sets of reflections have also been introduced and simultaneously fitted. The first set included the Bragg reflections of the main phase

¹ Supplementary data for this paper are available from the IUCr electronic archives (Reference: SH0134). Services for accessing these data are described at the back of the journal.

Table 1

High-resolution temperature-dependent neutron powder diffraction: experimental details.

Data collection					
Radiation type	Neutron				
Diffractometer	3T2, LLB				
Wavelength (Å)	1.2251				
Sample container	Vanadium can				
2θ range (°)	6–125.7				
2θ step scan (°)	0.05				
Monochromator	Ge (335)				
Sample environment	Cryostat (10 and 150 K)–Furnace (440 and 520 K)–None (290 K)				
Instrumental geometry	20 ³ He detectors				
Crystal data					
Chemical formula	PbHf _{0.8} Ti _{0.2} O ₃				
Chemical Formula weight	407.52				
μ _R	0.15				
T (K)	10	150	290	440	520
Cell setting	Rhombohedral	Rhombohedral	Rhombohedral	Rhombohedral	Cubic
Space group	R3c	R3c	R3c	R3c	Pm3̄m
a _{hex} (Å)	5.7827 (1)	5.7871 (1)	5.7943 (1)	5.8025 (2)	–
c _{hex} (Å)	14.2702 (4)	14.2735 (4)	14.2742 (5)	14.2648 (4)	–
a _{cub} (Å)	–	–	–	–	4.1072 (1)
V (Å ³)	413.26 (2)	413.98 (3)	415.04 (3)	415.94 (3)	69.28 (1)
Z	6	6	6	6	1
Refinement					
Background	Polynomial function				
Excluded regions	6–15; 109–125.7				
Full width at half maximum	Caglioti function				
Profile shape function	Pseudo-Voigt				
Structure refinement program	Fullprof (Rodriguez-Carvajal, 1990)				
Weighting scheme	w = 1/σ ² ; σ ² = y _i				
T (K)	10	150	290	440	520
No. of reflections	158	158	158	117	39
No. of parameters refined†	39	39	39	38	33
R _p	0.032	0.032	0.035	0.038	0.044
R _{wp}	0.040	0.041	0.044	0.050	0.055
R _{exp}	0.028	0.029	0.029	0.029	0.036
χ ²	2.02	2.00	2.28	3.00	2.37

$R_p = \sum |y_i - y_{ci}| / \sum y_i$; $R_{wp} = [\sum w_i (y_i - y_{ci})^2 / \sum w_i y_i^2]^{1/2}$. † Including the parameters refined for the additional phase of HfO₂.

PbHf_{0.8}Ti_{0.2}O₃, the intensities being calculated from a structural model. For the second set, the reflections from HfO₂, no structural model was fed into the refinement procedure and the experimental profiles were adjusted using a cell-constrained refinement only (pattern matching mode). Since the instrumental resolution of D1B is low, experimental profiles were modelled using a Gaussian profile shape function. Sample absorption and systematic errors were corrected, and the background was adjusted from a polynomial function.

Considering the numerous diffraction patterns collected over the temperature range 300–770 K, the program *Fullprof* (Rodriguez-Carvajal, 1990) ran in a sequential mode which consists of using the resulting refined parameters of the preceding pattern as the starting parameters for the next. This mode is an efficient procedure to follow the temperature dependence of various crystallographic parameters.

3. Structural description

In many rhombohedral distorted perovskites, the structural description can be performed in terms of very few parameters related to the octahedron tilt, octahedron distortion and

cation shifts. In the case of PbHf_{0.8}Ti_{0.2}O₃ the two rhombohedral phases F_{RL} and F_{RH} can be described in a common geometrical representation, allowing comparisons and defined from four structural parameters, e , d , s and t (Megaw & Darlington, 1975). The parameter e is related to the tilt angle ω , which indicates the rotation of the oxygen octahedra around the triad axis [$\tan \omega = 4(3)^{1/2}e$]. The distortion of the oxygen octahedra, keeping the triad axis symmetry and making the sizes of the upper and lower faces different, is described from the parameter d . Finally, the shifts of the Pb²⁺ and Hf⁴⁺/Ti⁴⁺ cations along the ferroelectric axis are respectively derived from the parameters s and t .

In the low-temperature phase F_{RL} , space group $R3c$, the oxygen octahedral tilting implies a ‘pseudo-cubic’ unit cell with doubled edge lengths. With respect to the hexagonal axes, the corresponding lattice parameters are $a_{\text{hex}} \simeq 5.78$ and $c_{\text{hex}} \simeq 14.27$ Å with $Z = 6$ (doubled hexagonal cell height). The atomic coordinates are given in Table 3 (Megaw & Darlington, 1975).

In the intermediate phase F_{RH} , space group $R3m$, there is no octahedron tilt and the parameter e is set to zero. The rotation vanishes, the doubled unit cell along the hexagonal axis is not necessary and the structural description should be

Table 2

Details of the neutron powder thermodiffraction experiment (given at 290 K).

Data collection	
Radiation type	Neutron
Diffraction	D1B, ILL
Wavelength (Å)	2.533
Sample container	Vanadium can
2θ range (°)	30.02–109.82
2θ step scan (°)	0.2
Monochromator	Pyrolytic graphite (002)
Instrumental geometry	400 ³ He cells
Sample environment	Furnace
Temperature range (K)	290–770
Crystal data	
Chemical formula	PbHf _{0.8} Ti _{0.2} O ₃
Chemical formula weight	407.52
μ _R	0.30
Cell setting	Rhombohedral
Space group	<i>R3c</i>
a _{hex} (Å)	5.7948 (2)
c _{hex} (Å)	14.276 (1)
V _{hex} (Å ³)	415.16 (6)
Z	6
Refinement	
Background	Polynomial function
Excluded regions	30.02–34.22
Full width at half maximum	Caglioti function
Profile shape function	Gaussian
Structure refinement program	<i>Fullprof</i> running in sequential mode (Rodriguez-Carvajal, 1990)
Weighting scheme	w = 1/σ ² ; σ ² = y;
No. of reflections	15
No. of parameters refined†	16
R _p	0.021
R _{wp}	0.027
R _{exp}	0.008
χ ²	10.9

† Including the parameters refined for the additional phase of HfO₂.

performed with lattice parameters $a_{\text{hex}} \approx 5.80$ and $c_{\text{hex}} \approx 7.13$ Å. However, in order to compare the two phases F_{RL} and F_{RH} , it is easiest to keep the structural model in the doubled hexagonal cell. The symmetry operators of space group *R3c* were used, but a restriction was inserted for O-atom positions, *i.e.* $y_{\text{O}} = 2x_{\text{O}}$. This restriction introduces mirror planes not given by the space group and containing the threefold axis and each O atom (Megaw & Darlington, 1975; Glazer *et al.*, 1978; Corker, Glazer, Whatmore *et al.*, 1998). Space groups *R3c* and *R3m* allow an arbitrary choice of the origin. With the O atoms forming a set of equally spaced planes normal to the triad axis, the origin is chosen midway between these planes, *i.e.* at the centre of mass of an oxygen octahedron.

In the structural refinements presented below, four atomic position parameters were refined for the phase F_{RL} ($z_{\text{Pb}} = 1/4 + s$, $z_{\text{Hf/Ti}} = t$, x_{O} and y_{O}) and only three for the phase F_{RH} ($z_{\text{Pb}} = 1/4 + s$, $z_{\text{Hf/Ti}} = t$ and $y_{\text{O}} = 2x_{\text{O}}$). With the choice of the origin, s and t give the cationic shifts relative to the oxygen octahedra. For the paraelectric cubic perovskite structure, the usual atomic positions described in space group *Pm3̄m* were checked in the refinement (Table 3).

Table 3

Structural descriptions given in the rhombohedral space groups *R3c* and *R3m* (in the hexagonal axes) and in the cubic space group *Pm3̄m* (Megaw & Darlington, 1975).

Space group	Atom	Site	x	y	z
<i>R3c</i>	Pb	6(a)	0	0	1/4 + s
	Hf/Ti	6(a)	0	0	t
	O	18(b)	1/6 – 2(e + d)	1/3 – 4d	1/12
<i>R3m</i> †	Pb	6(a)	0	0	1/4 + s
	Hf/Ti	6(a)	0	0	t
	O	18(b)	1/6 – 2d	1/3 – 4d	1/12
<i>Pm3̄m</i>	Pb	1(a)	0	0	0
	Hf/Ti	1(b)	1/2	1/2	1/2
	O	3(c)	0	1/2	1/2

† Description using the symmetry operators of space group *R3c* with a hexagonal cell of height $c_{\text{hex}} \approx 14$ Å.

4. High-resolution neutron powder diffraction

Taking into account the small amount of an additional phase of HfO₂, the corresponding diffracted intensities have been calculated from the monoclinic structural model given by Wang *et al.* (1992) in space group *P2₁/c*. Lattice constants, atomic coordinates and independent isotropic atomic displacements parameters were refined together with the scale factor. From the ratio of the scale factors of the two phases, a quantitative phase analysis has been performed (Hill & Howard, 1987): a fraction of 8.0% (± 0.5%) in mass of HfO₂ has been determined for all the temperatures.

4.1. Ferroelectric rhombohedral phases F_{RL} and F_{RH}

High-resolution neutron powder diffraction diagrams, collected at 10, 150 and 290 K, were fitted from the structural model described above. At the beginning of the refinement, the cell parameters, atomic positions and an overall isotropic atomic displacement parameter were simultaneously refined with the scale factor, the profile parameters and the polynomial function describing the background. Then, the chemical occupancy on the Hf/Ti site was optimized together with independent isotropic atomic displacement parameters. At the end of the refinements, the Hf chemical occupancy was equal to 0.80 (1), a value which is in good agreement with the EDS analyses. Structural results are given in Table 4 and the corresponding bond lengths are calculated in Table 5. Structural refinement including the two phases leads to satisfactory reliability factors: $R_{\text{Bragg}} = 0.021$ and $R_{\text{F}} = 0.013$ at 10 K; $R_{\text{Bragg}} = 0.024$ and $R_{\text{F}} = 0.016$ at 150 K; $R_{\text{Bragg}} = 0.031$ and $R_{\text{F}} = 0.025$ at 290 K. Fig. 1(a) shows the observed and calculated neutron diffraction profiles and their difference curve at 10 K.

Following the previous work performed on the parent compound PbHf_{0.4}Ti_{0.6}O₃ (Muller *et al.*, 1999), for which a cationic splitting has been evidenced on the Hf/Ti site, some attempts have been performed to separate Hf and Ti atoms (their atomic displacements parameters being constrained). Firstly, a shift δz has been introduced between the two cations, in the range –0.10 to +0.10. Compared with PbHf_{0.4}Ti_{0.6}O₃, no well marked minimum of the reliability factors *versus* δz was

observed and the atomic displacement parameters showed no significant variations. In a second step, the two atomic positions of Hf and Ti cations were independently refined: the resulting refinements bring to light a splitting, the Ti^{4+} cations drastically moving off-centre of the octahedra. This observation corroborates previous results obtained on the PZT

(Corker, Glazer, Whatmore *et al.*, 1998) or PHT series (Muller *et al.*, 1999). However, no significant improvement was obtained and the resulting cationic shifts do not present a relevant and physically acceptable thermal behaviour.

Another interesting point is related to the high value of the isotropic atomic displacement parameters associated with the heaviest atoms of the structure, *i.e.* Pb^{2+} cations. When anisotropic displacement parameters are refined, the fits are significantly improved ($R_{\text{Bragg}} = 0.019$ and $R_F = 0.012$ at 10 K; $R_{\text{Bragg}} = 0.021$ and $R_F = 0.013$ at 150 K; $R_{\text{Bragg}} = 0.026$ and $R_F = 0.021$ at 290 K) and disc-shaped ellipsoids with the smallest axis parallel to the ferroelectric axis are exhibited. This result seems to indicate a Pb disorder perpendicular to the ferroelectric axis in the F_{RL} phase. The anisotropic displacement parameters are not correlated with the other parameters since cationic shifts along the ferroelectric axis remain unchanged within the error bars. Such a phenomenon has already been observed in the rhombohedral phases of the PZT series (Glazer *et al.*, 1978; Corker, Glazer, Whatmore *et al.*, 1998; Ricote *et al.*, 1998) and was interpreted in terms of superimposed ‘nanoscale’ domains with various cation shifts in the pseudo-cubic directions $[1\bar{1}0]_{\text{cub}}$, $[10\bar{1}]_{\text{cub}}$ and $[01\bar{1}]_{\text{cub}}$ (Corker, Glazer, Whatmore *et al.*, 1998). A way to describe this disorder is to displace Pb atoms from their high-symmetry positions $(0, 0, z)$ to one of the six equivalent (x, y, z) positions, thus allowing the Pb atoms to shift not only along the ferroelectric axis but also perpendicularly to this direction. Using this description the refinements quickly converged with reliability factors very close to those obtained when anisotropic atomic displacements are refined. The resulting parameters are: $x_{\text{Pb}} = 0.018$ (1), $y_{\text{Pb}} = 0.011$ (7), $z_{\text{Pb}} = 0.2835$ (1) and $B_{\text{iso}}[\text{Pb}] = 0.34$ (3) \AA^2 at 10 K; $x_{\text{Pb}} = 0.026$ (1), $y_{\text{Pb}} = 0.015$ (4), $z_{\text{Pb}} = 0.2820$ (1) and $B_{\text{iso}}[\text{Pb}] = 0.52$ (4) \AA^2 at 150 K; $x_{\text{Pb}} = 0.031$ (2), $y_{\text{Pb}} = 0.021$ (4), $z_{\text{Pb}} = 0.2793$ (2) and $B_{\text{iso}}[\text{Pb}] = 1.15$ (6) \AA^2 at 290 K. These refinements provide realistic atomic displacement parameters and clearly show that the shifts perpendicular to the axis increase along with the temperature.

For the neutron diffraction pattern recorded at 440 K (Fig. 1*b*), the symmetry operators of the space group $R3c$ were used and the oxygen atomic positions x_{O} and y_{O} were constrained by the condition implying a structure factor equal to zero for the superstructure reflections. This restriction explains the extinction of the weak reflections arrowed in Fig. 1(*a*).

Introducing the structural model of the phase HfO_2 , the refinement leads to satisfactory

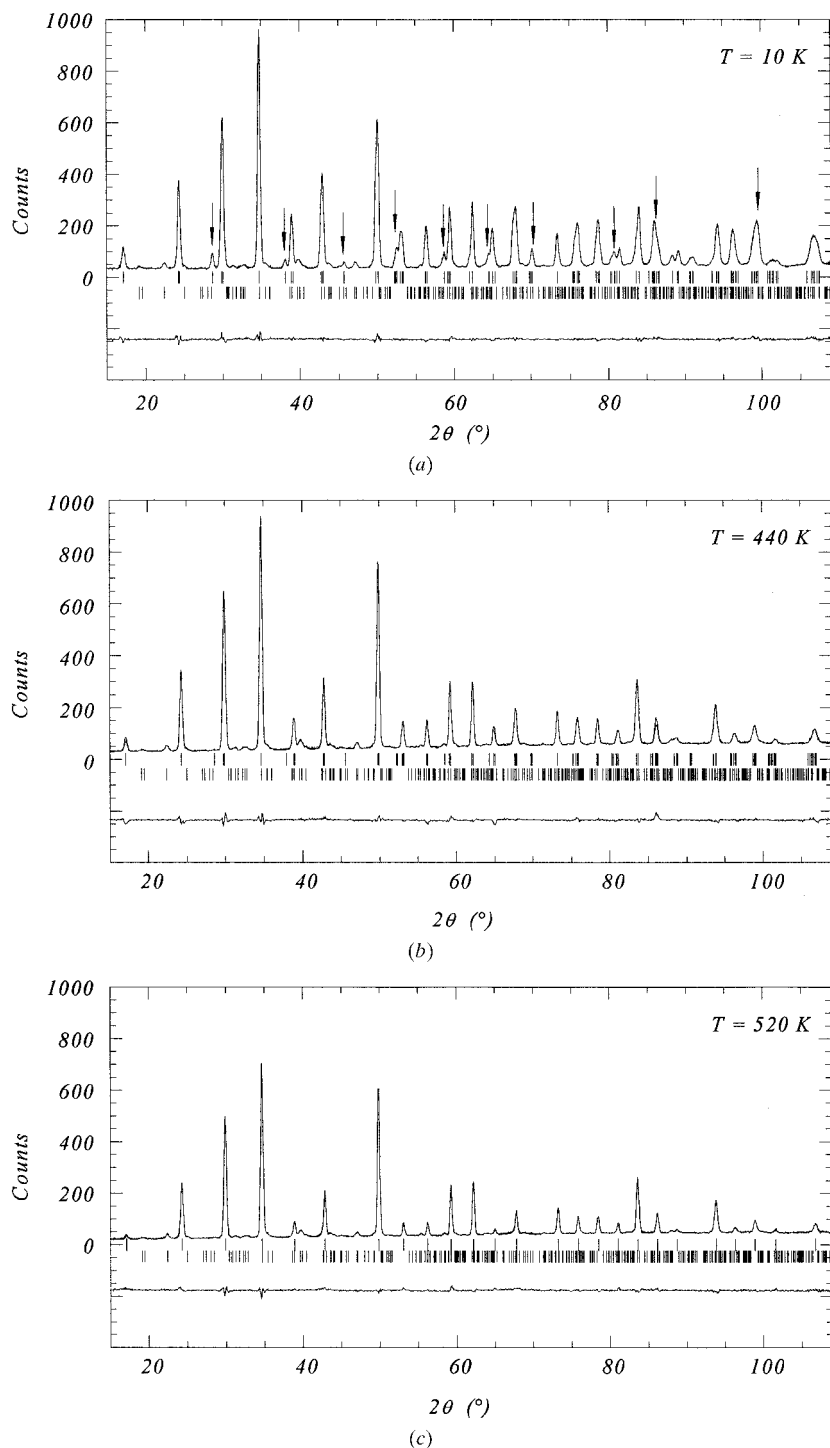


Figure 1
Observed and calculated neutron diffraction profiles and their difference curves for lead hafnate titanate at (a) 10, (b) 440 and (c) 520 K. Upper sticks correspond to the main phase of $\text{PbHf}_{0.8}\text{Ti}_{0.2}\text{O}_3$, lower sticks to the additional phase of HfO_2 .

Table 4

Fractional atomic coordinates, Hf/Ti occupancy and atomic displacement parameters resulting from the Rietveld refinement of $\text{PbHf}_{0.8}\text{Ti}_{0.2}\text{O}_3$ (with s.u.'s in parentheses).

The description $R3m$ is in space group $R3c$, constraining the oxygen position by $y_O = 2x_O$.

For anisotropic atomic displacements, the exponent term takes the form

$$T = \exp[-(1/4)(B^{11}h^2a^{*2} + B^{22}k^2b^{*2} + B^{33}l^2c^{*2} + 2B^{12}hka^*b^* + 2B^{13}hla^*c^* + 2B^{23}klb^*c^*)]$$

with $B_{\text{eq}} = (1/3)\Sigma_i B_i$; $R_{\text{Bragg}} = \Sigma_k |I_k - I_k^{\text{calc}}| / \Sigma_k I_k$; $R_F = \Sigma_k |(I_k)^{1/2} - (I_k^{\text{calc}})^{1/2}| / \Sigma_k (I_k)^{1/2}$.

	$R3c$			$R3m$	$Pm\bar{3}m$
	10 K	150 K	290 K	440 K	520 K
$z_{\text{Pb}} = 1/4 + s$	0.2835 (1)	0.2821 (1)	0.2793 (1)	0.2734 (2)	–
$z_{\text{Hf/Ti}} = t$	0.0126 (1)	0.0121 (1)	0.0114 (2)	0.0105 (2)	–
x_O	0.1427 (2)	0.1458 (2)	0.1525 (2)	0.1722 (4)	–
y_O	0.3461 (2)	0.3456 (2)	0.3448 (3)	$2x_O$	–
B^{11} [Pb] (\AA^2)	1.04 (2)	1.85 (3)	3.47 (3)	5.53 (4)	4.37 (4)
B^{33} [Pb] (\AA^2)	0.35 (2)	0.57 (2)	1.14 (2)	2.53 (3)	B^{11}
B_{eq} [Pb] (\AA^2)	0.58 (2)	1.00 (2)	1.92 (3)	3.53 (6)	4.37 (4)
B_{iso} [Hf/Ti] (\AA^2)	0.03 (4)	0.06 (2)	0.18 (2)	0.32 (3)	0.29 (3)
B^{11} [O] (\AA^2)	–	–	–	–	0.86 (2)
B^{33} [O] (\AA^2)	–	–	–	–	3.67 (1)
B_{iso} [O] or B_{eq} [O] (\AA^2)	0.67 (2)	0.83 (2)	1.28 (2)	1.96 (2)	2.73 (3)
Hf chemical occupancy	0.80 (1)	0.80 (1)	0.80 (1)	0.81 (1)	0.79 (1)
R_{Bragg}	0.019	0.021	0.026	0.034	0.039
R_F	0.012	0.013	0.021	0.027	0.025
$s' = s \times c_{\text{hex}}$ (\AA)	0.478 (2)	0.457 (2)	0.418 (2)	0.333 (3)	–
$t' = t \times c_{\text{hex}}$ (\AA)	0.180 (2)	0.172 (2)	0.163 (3)	0.150 (3)	–
$d \sim 10^2$	–0.32 (2)	–0.31 (2)	–0.29 (3)	–0.28 (4)	0
$e \times 10^2$	1.52 (6)	1.35 (7)	1.00 (9)	0	0
ω ($^\circ$)	6.0 (2)	5.3 (2)	3.9 (3)	0	0
$\zeta \times 10^2$	0.19	0.25	0.33	0.36	0
P_S ($\mu\text{C cm}^{-2}$)	38.9	37.3	34.4	29.2	0

Table 5

Bond lengths (\AA).

NB Indexes used to distinguish O atoms: l for lower faces of the oxygen octahedra and u for upper faces.

	10 K	150 K	290 K	440 K	520 K
Hf/Ti– O_u	2.01 ($\times 3$)	2.01 ($\times 3$)	2.02 ($\times 3$)	2.10 ($\times 3$)	2.05 ($\times 6$)
Hf/Ti– O_l	2.12 ($\times 3$)	2.11 ($\times 3$)	2.11 ($\times 3$)	2.02 ($\times 3$)	–
O_l – O_l	2.80 ($\times 3$)	2.90 ($\times 12$)			
O_u – O_u	3.02 ($\times 3$)	3.01 ($\times 3$)	3.00 ($\times 3$)	3.00 ($\times 3$)	–
O_l – O_u	2.92 ($\times 6$)	2.91 ($\times 6$)	2.91 ($\times 6$)	2.91 ($\times 6$)	–
Pb–O	2.49 ($\times 3$)	2.51 ($\times 3$)	2.54 ($\times 3$)	2.61 ($\times 3$)	2.90 ($\times 12$)
	2.76 ($\times 3$)	2.78 ($\times 3$)	2.81 ($\times 3$)	2.92 ($\times 6$)	–
	3.10 ($\times 3$)	3.08 ($\times 3$)	3.04 ($\times 3$)	–	–
	3.35 ($\times 3$)	3.33 ($\times 3$)	3.29 ($\times 3$)	3.22 ($\times 3$)	–

reliability factors, *i.e.* $R_{\text{Bragg}} = 0.034$ and $R_F = 0.028$. Observed, calculated and difference patterns are presented in Fig. 1(b). As for the F_{RL} phase, we have tried to reduce the mean-square atomic displacements associated with the Pb nucleus in splitting its crystallographic site. However, applying this procedure no convergence could be reached. In the study of the F_{RL} – F_{RH} composition-induced phase transition in the PZT series (Corker, Glazer, Whatmore *et al.*, 1998), a similar phenomenon has been reported in the compound $\text{PbZr}_{0.6}\text{Ti}_{0.4}\text{O}_3$, which crystallizes in the F_{RH} form. Following this result and the present study, one can assume that a correlation exists between the oxygen octahedra rotation and the Pb disorder perpendicular to the threefold axis.

From the atomic coordinates given in Table 4 the parameters s , t , d and e were derived for the two ferroelectric

phases F_{RL} and F_{RH} . Regarding the octahedron deformations, the extracted values of d and e (Table 4) compare well with those obtained by Glazer *et al.* (1978) and Ito *et al.* (1983) on $\text{PbZr}_{0.9}\text{Ti}_{0.1}\text{O}_3$, by Noheda *et al.* (1996) on an Nb-doped Zr-rich PZT compound and more recently by Corker, Glazer, Kaminsky *et al.* (1998) on the series $\text{PbZr}_{1-x}\text{Ti}_x\text{O}_3$ with x ranging from 0.12 to 0.40. The parameter d slightly decreases from -0.0032 at 10 K to -0.0029 at 290 K, the negative value signifying that the upper face of the octahedron is larger than the lower. The bond lengths given in Table 5 corroborate this interpretation since the O_l – O_l distances on the lower face are largely smaller than the O_u – O_u distances on the upper face. On the other hand, the tilt angle ω was deduced from the parameter e refined in the phase F_{RL} . Between 10 and 290 K the rotation angle decreases from 6.0 (2) to 3.9 (3) $^\circ$. In the intermediate phase F_{RH} , in agreement with the extinction of superstructure reflections, the octahedra rotation disappears, but the octahedral distortion subsists ($d = -0.0028$ at 440 K).

Concerning the Pb^{2+} and $\text{Hf}^{4+}/\text{Ti}^{4+}$ displacements, the two parameters s' and t' directly give the cation shifts (expressed in \AA) along the ferroelectric axis relative to the oxygen octahedron (Table 4). The $\text{Hf}^{4+}/\text{Ti}^{4+}$ displacements are directed from the lower octahedron face to the upper, this being consistent with the negative value of the parameter d (the smaller oxygen triangle corresponds to the face more distant from the shifted cations).

From the parameter t' , which slightly decreases from 0.18 to 0.15 \AA between 10 and 440 K, it is shown that the pseudonucleus Hf/Ti is much closer to the centre of the oxygen octahedron than Ti in the tetragonal PbTiO_3 , *i.e.* 0.30 \AA along the $[001]_{\text{tetra}}$ axis (Shirane *et al.*, 1956; Glazer & Mabud, 1978), but this displacement is quite similar to that of Hf atoms in the orthorhombic PbHfO_3 , *i.e.* 0.17 \AA along the $[100]_{\text{orth}}$ orthorhombic direction (Corker, Glazer, Kaminsky *et al.*, 1998; Madigou *et al.*, 1999).

On the other hand, the Pb^{2+} shifts along the ferroelectric axis which vary in the range 0.48–0.33 \AA from 10 to 440 K are greater than $\text{Hf}^{4+}/\text{Ti}^{4+}$ ones. The Pb displacements are similar

to those observed either in $\text{PbHf}_{0.4}\text{Ti}_{0.6}\text{O}_3$ (Muller *et al.*, 1999) or in PbTiO_3 (Shirane *et al.*, 1956; Glazer & Mabud, 1978). The spread of the Pb–O bond lengths (Table 5) show that the Pb atoms are displaced from the distorted 12-fold-coordinated site which is cubic in the case of the idealized perovskite structure.

4.2. Paraelectric cubic phase P_C

A full profile fitting refinement was also performed on the diffraction pattern registered at 520 K (Fig. 1c). The diffracted intensities were calculated from the idealized perovskite-type structure corresponding to a non-distorted octahedral model (Table 3). After preliminary refinement to establish the scale factor and the profile parameters, several cycles were performed in refining three independent isotropic atomic displacements parameters together with the composition ratio x . The refinement leads to unsatisfactory reliability factors ($R_{\text{Bragg}} = 0.068$ and $R_F = 0.054$) even if the Hf chemical occupancy was determined to be equal to 0.79 (1), a value in good agreement with previous refinements. When anisotropic oxygen displacement parameters were refined, the reliability factors drastically decreased ($R_{\text{Bragg}} = 0.039$ and $R_F = 0.025$). The resulting oxygen displacement parameters exhibit an anisotropy with disc-shaped ellipsoids parallel to the faces of the cube.

Furthermore, an abnormally high value of the isotropic atomic displacements parameter B_{iso} [Pb] associated with the Pb nuclei is also observed in this high-temperature paraelectric phase. Similar phenomena have already been noticed in the high-temperature phase of the parent compound $\text{PbHf}_{0.4}\text{Ti}_{0.6}\text{O}_3$ (Muller *et al.*, 1999) and in other perovskite-type structures (Nelmes *et al.*, 1990; Kwapulinski *et al.*, 1994; Malibert *et al.*, 1997). When the Pb^{2+} cation is moved from its high-symmetry position (0, 0, 0) to the (0.05, 0.05, 0) position,

the refinement is slightly improved ($R_{\text{Bragg}} = 0.038$) and the isotropic atomic displacements parameter B_{iso} [Pb] drastically decreases from 4.4 to 1.8 Å². This characteristic is probably related to a dynamic or static disorder around the Pb high-symmetry position.

5. Neutron powder thermodiffraction

From the sequential refinements of a number of structural parameters, some quantitative results have been extracted from the neutron powder thermodiffraction data. To avoid correlations, only few parameters were simultaneously refined: cell parameters, atomic positions and an overall atomic displacements parameter B_{overall} of the phase $\text{PbHf}_{0.8}\text{Ti}_{0.2}\text{O}_3$, together with the monoclinic lattice constants of HfO_2 . The two rhombohedral structures of the phases F_{RL} and F_{RH} were refined from the crystallographic model given in space group $R3c$ (Table 3). Above the $F_{\text{RL}}-F_{\text{RH}}$ transition, the constraint on the oxygen atomic coordinates was applied ($y_{\text{O}} = 2x_{\text{O}}$). Finally, the high-temperature cubic phase P_C was described from the idealized perovskite-type structure.

Fig. 2 shows the temperature-dependent evolution of the diffraction patterns between 350 and 580 K. It clearly exhibits the occurrence of the first phase transition through the vanishing of the weak superstructure reflections (at $2\theta \simeq 62^\circ$ for instance), the second one being noticeable from the strong variations in the intensities of the main reflections (at $2\theta \simeq 36^\circ$).

5.1. Lattice expansion

From the sequential data treatment, the lattice expansion has been studied as a function of the temperature. In order to compare the thermal behaviour of the various phases (rhombohedral and cubic), the cell parameters are given with reference to the crystallographic axes, either hexagonal (Figs. 3a and 3c) or rhombohedral (Fig. 3b), corresponding to the low-temperature phase F_{RL} . Important changes are observed over the whole temperature range, especially between the two phase transitions which clearly appear at 415 and 520 K. Below 415 K, in the phase F_{RL} , the hexagonal cell volume is expanded even if the c_{hex} axis shows a slight contraction. Above 520 K, in the paraelectric phase, the thermal expansion exhibits a typical linear behaviour along with the temperature. In contrast, in the intermediate phase F_{RH} , a strong shrinking of the structure occurs along the ferroelectric axis $[001]_{\text{hex}}$, although a_{hex} presents a regular evolution. These important changes lead to a negative thermal expansion noticeable from the thermal dependence of the hexagonal unit-cell volume (Fig. 3c).

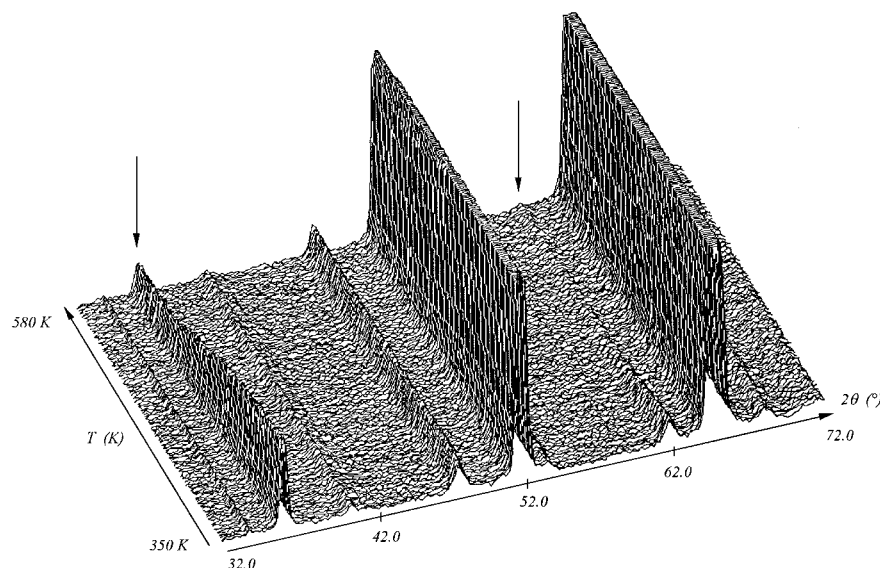


Figure 2

Temperature dependence of the neutron powder diffraction patterns (in the range 32–72° in 2θ) from 350 to 580 K. For clarity, the intensities of the strong main reflections have been truncated.

In Fig. 3(b) the rhombohedral angle reaches a value of 59.75° at 300 K and increases gradually with increasing temperature. From this evolution, the ferroelectric to-paraelectric transition seems to be continuous and the F_{RL} – F_{RH} phase transition is quite undetectable.

5.2. Structural parameters

From structural refinements the evolution of the oxygen octahedral deformations has been analysed as a function of temperature. Fig. 4(a) firstly shows the variation of the parameter $-d$, which describes the distortion of the oxygen

triangles perpendicular to the triad axis. As previously observed from high-resolution neutron powder diffraction data, the negative sign of d indicates that the upper face is larger than the lower one. Furthermore, the decrease in d with increasing temperature shows that the oxygen triangles are less and less distorted until the F_{RH} – P_C phase transition. Then, in the cubic phase P_C , the octahedra are regularly shaped. However, one can notice a slight discrepancy between the values determined by the two data sets which can be explained by the low resolution of D1B, providing less accurate atomic coordinates. Furthermore, Fig. 4(a) also shows the thermal evolution of the parameter e , which is related to the rotation of the octahedral faces around the triad axis. This parameter decreases continuously with increasing temperature, indicating a slow vanishing of the tilt angle ω until the F_{RL} – F_{RH} phase transition. Above 415 K, only the distortion of the oxygen triangles persists.

Besides the oxygen octahedral deformations, the evolution of the cation shifts has been studied as a function of the temperature (Fig. 4b). The two parameters s and t decrease along with the temperature, but the evolution of s seems to be more regular than t . Indeed, the parameter t decreases smoothly until the first phase transition and then drops abruptly to zero at the ferroelectric to-paraelectric phase transitions.

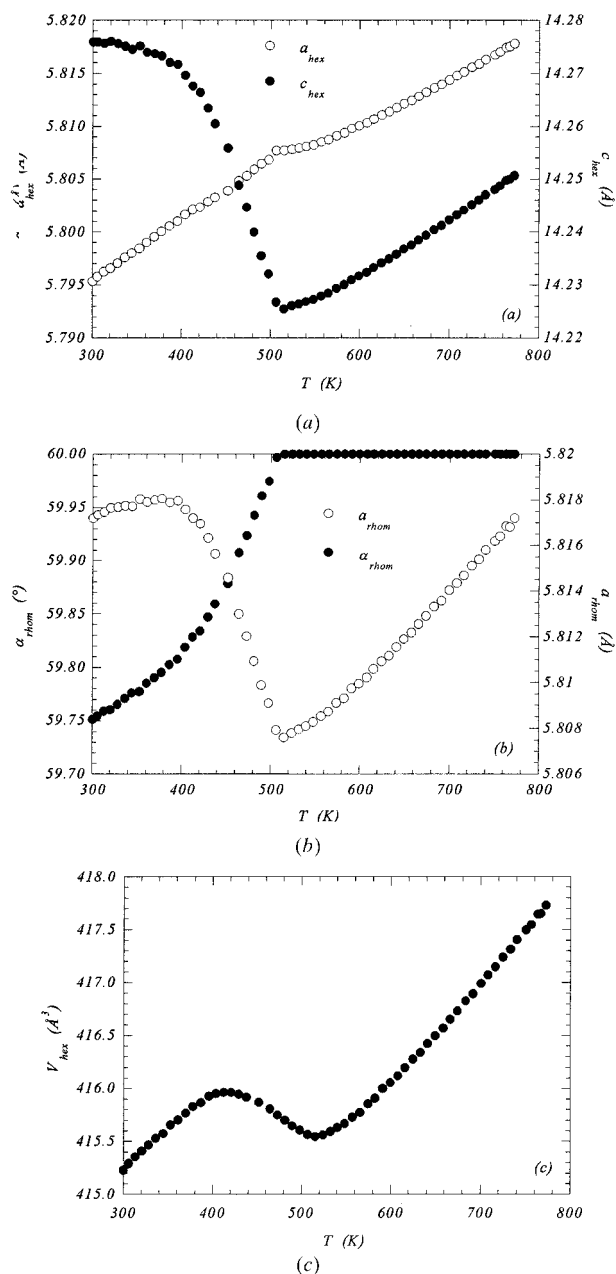


Figure 3 Temperature-dependent evolution of the cell parameters given (a) in the hexagonal axes and (b) in the rhombohedral axes. The hexagonal cell volume is plotted as a function of the temperature in (c).

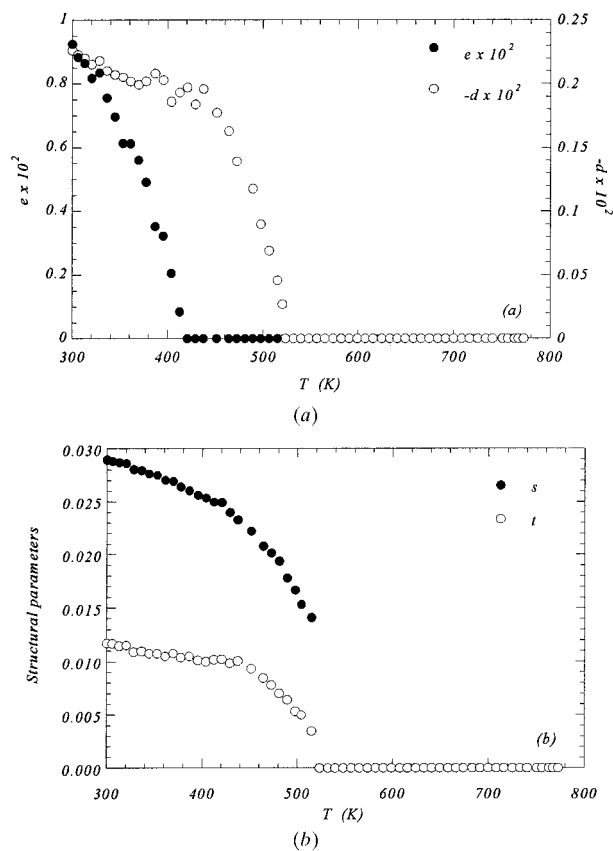


Figure 4 Evolution with temperature of the parameters d and e describing (a) the octahedral deformations and (b) the parameters s and t related to the cation shifts along the ferroelectric axis.

5.3. Static and dynamic disorder

An overall isotropic atomic displacement parameter B_{overall} , taking into account the mean-square displacements of all the atoms of the structure, has been refined based on temperature together with the other structural parameters. A plot of this parameter *versus* temperature is given in Fig. 5. It appears to increase linearly between 300 and 520 K and above 520 K a change in slope occurs, with a smaller increase with temperature. The temperature at which this deviation is observed corresponds to the ferroelectric-to-paraelectric phase transition. Therefore, the thermal behaviour of this parameter shows low- and high-temperature regions associated with the ferroelectric and paraelectric domains, respectively. In fact, the atomic displacement parameters can be separated into two components, *i.e.* static and thermal contributions: $B^{\text{exp}} = B^{\text{static}} + B^{\text{thermal}}$ (Willis, 1973). Therefore, at $T = 0$ K, only the static contribution persists. In our case, the extrapolated values at 0 K of the two regimes (guidelines depicted in Fig. 5) seem to indicate a static contribution only for the paraelectric domain: the value at 0 K is of $\sim 1.7 \text{ \AA}^2$, corresponding roughly to a static displacement of $\sim 0.15 \text{ \AA}$.

This peculiar behaviour characterizes a large static local disorder in the high-temperature cubic phase P_C . Considering the results developed in §4.2, it is probably essentially due to Pb atoms which present a strong disorder in the paraelectric phase. On the other hand, the disorder on the Pb sites in the ferroelectric phases, mentioned in §4.1, has been shown to increase with temperature, thus indicating a possible dynamic contribution. This behaviour could explain why the extrapolation of the ferroelectric region gives no or a very weak static contribution in Fig. 5. However, further experimental evidence is needed to ascertain if the displacements in the ferroelectric region are predominately dynamic.

6. Discussion

From the results presented in §4 and §5, some physical parameters have been derived from the hexagonal cell parameters and structural parameters. In the following the experimental

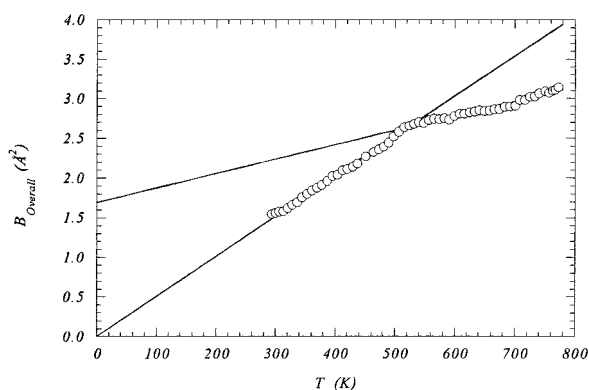


Figure 5
Plot *versus* temperature of the overall atomic displacement parameters. Guidelines show fitting to high-temperature and low-temperature regimes. Extrapolations at 0 K indicate the static contribution.

points obtained from the treatment of the diffraction data collected on the instrument 3T2 are indicated by arrows in the figures, the remaining points corresponding to the sequential analysis performed on the data registered on the diffractometer D1B.

6.1. Octahedral tilts and deformations

Using the relation $\tan \omega = 4(3)^{1/2}e$, the tilt angle ω derives directly from the structural parameter e . Its thermal evolution is plotted in Fig. 6. The angle ω exhibits a smooth decrease with temperature and seems to indicate a continuous transition between the two rhombohedral phases F_{RL} and F_{RH} . The disappearance of the oxygen octahedral rotation in the intermediate ferroelectric phase is related to the vanishing of the superstructure reflections evidenced in Fig. 2.

The tilt angle and the hexagonal cell parameters (with a hexagonal cell of height $c_{\text{hex}} \simeq 14 \text{ \AA}$) are coupled through an additional parameter ζ , called *octahedron strain* (Megaw & Darlington, 1975), which expresses the flattening or elongation of the oxygen octahedra along the triad axis. This parameter takes the form

$$\zeta = [c_{\text{hex}}/a_{\text{hex}}(6)^{1/2}] \cos \omega - 1.$$

For each temperature, this parameter has been calculated and its thermal evolution from 10 to 770 K is presented in Fig. 7. In the paraelectric cubic phase P_C , the octahedra are regularly shaped and $\zeta = 0$. Below 520 K the octahedral strain reaches positive values corresponding to an elongation of the octahedra along the triad axis. Its thermal behaviour reveals two regimes on both sides of the $F_{\text{RL}}-F_{\text{RH}}$ phase transition: from 10 to ~ 400 K, the strain gradually increases along with the temperature and then drops abruptly to be equal to zero at the second phase transition. As reported by Megaw & Darlington (1975), for many other perovskite-type structures the octahedron strains are generally negative (flattening along the triad axis) and decrease when the tilt angle ω decreases. In our case, in the ferroelectric phase F_{RL} the parameter ζ increases, although the tilt angle decreases (Fig. 6). This phenomenon

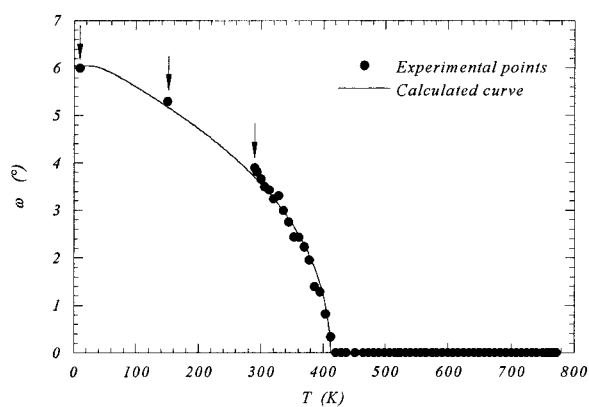


Figure 6
Experimental variation of the oxygen octahedron tilt angle ω with the temperature and calculated curve obtained from the generalized effective-field theory.

has also been observed on the PZT series when the F_{RH} phase is approached by decreasing the Zr content (Corker, Glazer, Whatmore *et al.*, 1998).

6.2. Cation displacements

For the two polar space groups $R3m$ and $R3c$, the shifts of the Pb^{2+} and Hf^{4+}/Ti^{4+} cations along the ferroelectric axis with respect to the oxygen octahedral centre (represented by the parameters s' and t') have been studied from 10 to 770 K (Fig. 8). Following the results developed in §4, the Pb^{2+} cations are more largely displaced than the Hf/Ti pseudo-nuclei. Their thermal behaviours indicate a smooth decrease in the low-temperature rhombohedral phase and then a more abrupt one in the intermediate phase F_{RH} . The non-vanishing of the parameter s' at 520 K can probably be associated with the static disorder on the Pb site evidenced in the paraelectric phase. One can suppose that a local polarization exists in one unit, but with the cations being statistically disordered, the long-range order (over a few unit cells) imposes a non-polar crystal.

6.3. Spontaneous polarization P_S

The cation shifts being directly related to the ferroelectric character of the perovskite-type structures means that polarization due to the relative ion displacements can be estimated. This polarization is proportional to $\sum_i(\delta z_i q_i/V)$, where δz_i is the shift along the ferroelectric axis of the i th ion carrying a charge q_i and V the volume of the unit cell. Our calculation is based on the assumption of a purely ionic crystal and neglects the electronic polarization. However, our values compare well with those calculated by Ito *et al.* (1983) and the difference between our calculated spontaneous polarizations and those measured on Zr-rich PZT for instance is usually small (Glazer *et al.*, 1978). Besides, to discuss the character of the transition it is sufficient to have the relative variation of the polarization as a function of temperature.

Fig. 9 shows the thermal evolution of the spontaneous polarization calculated from the structural parameters. Following the temperature-dependent evolution of the cation

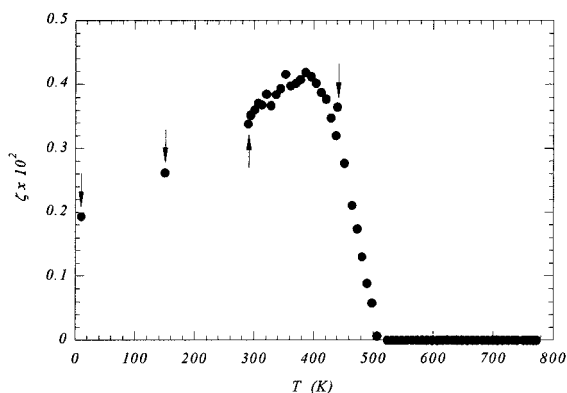


Figure 7
Thermal evolution of the octahedron strain ζ expressing the flattening or elongation of the oxygen octahedra along the triad axis.

shifts, the spontaneous polarization slowly decreases in the low-temperature phase F_{RL} and rapidly vanishes in the intermediate phase. Above 520 K, P_S is equal to zero, in agreement with the paraelectric state. Furthermore, the polarization presents no change at the onset of the tilting F_{RL} – F_{RH} transition, but the small discontinuity of derivatives associated with cation-shift thermal evolution (Fig. 8) could indicate a probable weak correlation between the octahedron tilt and the cation shifts.

6.4. Nature of the phase transitions

6.4.1. Effective-field theory. Previous works (Noheda *et al.*, 1995; Cereceda *et al.*, 1997) have shown that in the mixed system $PbZr_{1-x}Ti_xO_3$, the behaviour of the spontaneous polarization and the oxygen octahedral tilt angle ω could be analysed from a generalized effective-field theory.

To describe the temperature dependence of the polarization order parameter p_S , the effective field E_{eff} is expanded in powers of the polarization P

$$E_{eff} = E + \beta.P + \gamma.P^3 + \delta.P^5 + \dots,$$

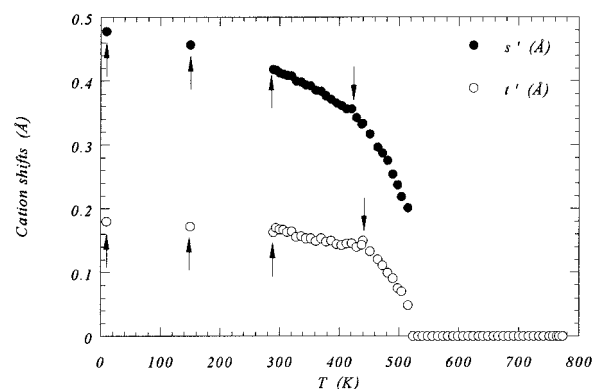


Figure 8
Thermal evolution of the cation shifts (given in Å) with respect to the oxygen octahedral centre: s' and t' are associated with the Pb^{2+} and Hf^{4+}/Ti^{4+} cations displacements, respectively.

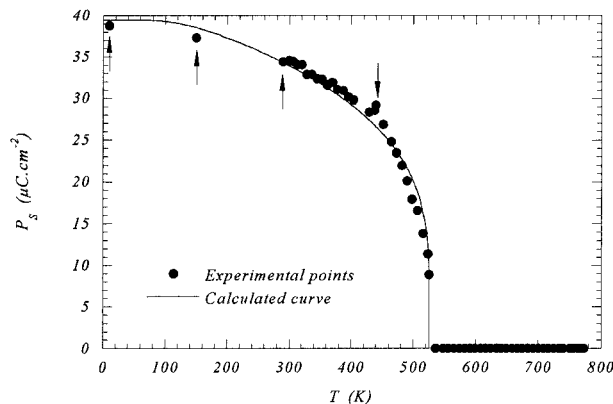


Figure 9
Spontaneous polarization calculated from the cell parameters and cation shifts. Its thermal behaviour is given between 10 and 770 K. The continuous line corresponds to the calculated curve from the effective-field theory.

where E is an external field and β , γ and δ are constant coefficients.

Considering N dipoles per unit volume, carrying an elementary dipole moment μ , using the dimensionless variables $e_S = E/(\beta N\mu)$, $p_S = P/N\mu$ and substituting $T_c = (\beta N\mu^2)/k_B$ (k_B is Boltzmann's constant), $g = (\gamma N^2\mu^2)/\beta$ and $h = (\delta N^4\mu^4)/\beta$, the authors established the following equation-of-state (Cereceda *et al.*, 1997)

$$e_S = (T/T_c) \tanh^{-1} p_S - p_S(1 + g.p_S^2 + h.p_S^4 + \dots). \quad (1)$$

On the other hand, a similar formalism has been used to describe the temperature dependence of the tilt order parameter $\eta_S(T)$, the effective torsional field X_{eff} being expanded in powers of the net staggered tilt per unit volume θ_t

$$X_{\text{eff}} = X + \beta'\theta_t + \gamma'\theta_t^3 + \delta'\theta_t^5 + \dots,$$

where β' , γ' and δ' are constant coefficients. The equation-of-state in dimensionless variables is then

$$x_S = (T/T_{\text{ct}}) \tanh^{-1} \eta_S - \eta_S(1 + g_t.\eta_S^2 + h_t.\eta_S^4 + \dots), \quad (2)$$

where $x_S = X/(\beta'N^2\omega)$; N' is the number of units of two oxygen octahedra tilted in the sequence or in the opposite sequence ($-\omega$, $+\omega$); $\eta_S = \theta_t/(N'2\omega)$; $T_{\text{ct}} = [\beta'N'(2\omega)^2]/k_B$; $g_t = [\gamma'N'^2(2\omega)^2]/\beta'$; $h_t = [\delta'N'^4(2\omega)^4]/\beta'$.

Having detailed neutron diffraction results over a large temperature range, it seemed interesting to apply the same generalized effective-field approach for analysing both tilt and polarization order parameters implied in the two transitions $F_{\text{RL}}-F_{\text{RH}}$ and $F_{\text{RH}}-P_C$ undergone in the compound $\text{PbHf}_{0.8}\text{Ti}_{0.2}\text{O}_3$.

6.4.2. Tilt order parameter. Fig. 6 shows the thermal behaviour of the tilt angle ω determined from our neutron powder diffraction data. The theoretical curve (full line) is calculated from (2) with $x_S = 0$. To adjust the experimental points we have used a fitting procedure, based on a least-squares minimization, requiring the tilt angle θ_t at $T = 0$ K and the Curie temperature T_{ct} (not known experimentally), and in which g_t and h_t are refined. The best adjustment was obtained for a tilt angle of 6.04° at 0 K and a temperature $T_{\text{ct}} = 412$ K. The second-order character of the transition is attested by the gradual decrease of ω with increasing temperature. More formally, the continuous character of this transition is confirmed by the negative value of the parameter $g_t = -0.34$ (10) [$h_t = -0.36$ (26)]. Indeed the value $g_t = 1/3$ corresponds to a tri-critical point, which is the borderline between a second-order transition ($g_t < 1/3$) and a first-order transition ($g_t > 1/3$). Besides, for the tilt-angle order parameter the Curie temperature T_{ct} is equal to the transition temperature T_0 ($T_{\text{ct}} = T_0 = 412$ K), as usual, in a second-order transition.

6.4.3. Polarization order parameter. From the calculated spontaneous polarizations, a theoretical curve (full line on Fig. 9) has been calculated from (1) with $e_S = 0$ (no external electrical field). At first sight we cannot predict if the polarization goes continuously to zero at the transition temperature. Therefore, a fitting procedure, similar to that used for the tilt-order parameter, was used. It requires polarization at 0 K and the Curie temperature T_c . From the best fit we can

conclude that the phase transition is 'weakly' first order: the refined parameter equal to 0.42 (6) is larger than the tri-critical point value of 1/3 and T_c (525.0 K) is very close to the transition temperature T_0 (525.5 K). The spontaneous polarization at 0 K is $39.4 \mu\text{C cm}^{-2}$. Thus, one can propose the existence of a tri-critical point in the PHT series for a composition x slightly larger than 20%. This result agrees well with the prediction of Cereceda *et al.* (1997) of a tri-critical point at $x = 0.26$ in the homologous PZT solid solution.

In conclusion, in the PHT series for the composition $x = 0.20$, the transition associated with the octahedral tilting is clearly second-order and the transition associated with polarization is weakly first-order.

7. Conclusions

Structural investigations of the phase transitions occurring in the compound $\text{PbHf}_{0.8}\text{Ti}_{0.2}\text{O}_3$ have been performed from temperature-dependent neutron powder diffraction. The following results have been found.

(i) This compound undergoes two phase transitions at 415 and 520 K. The former, related to the vanishing of the octahedral tilt around the triad axis, can be associated with a second-order phase transition, whereas the latter, separating the ferroelectric and paraelectric regions, is weakly first order in nature. The character of the phase transitions has been determined from an effective-field theory.

(ii) Neutron powder diffraction is a well suited technique to the localization of O atoms and is very sensitive to octahedral deformations. Our refinements have put forward very interesting thermal evolutions of the tilt angle ω and octahedron strain ζ . Contrary to the observations made in the usual perovskite-type structures, the octahedron strain determined in the ferroelectric F_{RL} phase increases when the tilt angle decreases.

(iii) A strong disorder on the Pb crystallographic sites has been evidenced in both ferroelectric and paraelectric regions. In the low-temperature ferroelectric phase F_{RL} , a disorder perpendicular to the ferroelectric axis is observed, whereas in the cubic paraelectric phase P_C the disorder can be described by displacing the Pb atoms from their high-symmetry position (0, 0, 0) to one of the 12 equivalent ($x, x, 0$) positions.

References

- Caglioti, G., Paoletti, A. & Ricci, F. P. (1958). *Nucl. Instrum.* **3**, 223–228.
- Cereceda, N., Noheda, B., Iglesias, T., Fernandez-del-Castillo, J. R., Gonzalo, J. A., Duan, N., Wang, Y. L., Cox, D. E. & Shirane, G. (1997). *Phys. Rev. B*, **55**, 6174–6179.
- Corker, D. L., Glazer, A. M., Kaminsky, W., Whatmore, R. W., Dec, J. & Roleder, K. (1998). *Acta Cryst.* **B54**, 18–28.
- Corker, D. L., Glazer, A. M., Whatmore, R. W., Stallard, A. & Fauth, F. (1998). *J. Phys.* **10**, 6251–6269.
- Favotto, C., Margaillan, A. & Roubin, M. (1996). *Ann. Chim. Fr.* **21**, 13–24.
- Glazer, A. M. & Mabud, S. A. (1978). *Acta Cryst.* **B34**, 1065–1070.
- Glazer, A. M., Mabud, S. A. & Clarke, R. (1978). *Acta Cryst.* **B34**, 1060–1065.

- Hill, R. J. & Howard, C. J. (1987). *J. Appl. Cryst.* **20**, 467–474.
- Ito, H., Shiozaki, Y. & Sawaguchi, E. (1983). *J. Phys. Soc. Jpn.*, **52**, 913–919.
- Jaffe, B., Cook, W. R. & Jaffe, H. (1971). *Piezoelectric Ceramics*. London: Academic Press.
- Jaffe, B., Roth, R. S. & Marzullo, S. (1955). *J. Res. Natl Bur. Stand.* **55**, 239–254.
- Kwapulinski, J., Pawelczyk, M. & Dec, J. (1994). *J. Phys.* **6**, 4655–4659.
- Madigou, V., Baudour, J.-L., Bouree, F., Favotto, C., Roubin, M. & Nihoul, G. (1999). *Philos. Mag. A*, **79**, 847–858.
- Malibert, C., Dkhil, B., Kiat, J.-M., Durand, D., Bérrar, J.-F. & Spasojevic de Biré, A. (1997). *J. Phys.* **9**, 7485–7500.
- Megaw, H. D. & Darlington, C. N. W. (1975). *Acta Cryst.* **A31**, 161–173.
- Muller, C., Baudour, J.-L., Madigou, V., Bouree, F., Kiat, J.-M., Favotto, C. & Roubin, M. (1999). *Acta Cryst.* **B55**, 8–16.
- Nelmes, J., Piltz, R. O., Kuhs, W. F., Tun, Z. & Restori, R. (1990). *Ferroelectrics*, **108**, 165–170.
- Noheda, B., Cereceda, N., Iglesias, T., Lifante, G., Gonzalo, J. A., Chen, H. T. & Wang, Y. L. (1995). *Phys. Rev. B*, **51**, 16388–16391.
- Noheda, B., Iglesias, T., Cereceda, N., Gonzalo, J. A., Chen, H. T., Wang, Y. L., Cox, D. E. & Shirane, G. (1996). *Ferroelectrics*, **184**, 251–255.
- Ricote, J., Corker, D. L., Whatmore, R. W., Impey, S. A., Glazer, A. M., Dec, J. & Roleder, K. (1998). *J. Phys.* **10**, 1767–1786.
- Rodriguez-Carvajal, J. (1990). *Fullprof. A Program for Rietveld Refinement and Pattern Matching Analysis*. Abstracts of the Satellite Meeting on Powder Diffraction of the XVth Congress of the International Union of Crystallography, p. 127.
- Shirane, G., Pepinsky, R. & Frazer, B. C. (1956). *Acta Cryst.* **9**, 131–140.
- Viehland, D. (1995). *Phys. Rev. B*, **52**, 778–791.
- Wang, J., Li, M. R. & Stevens, R. (1992). *J. Mater. Sci.* **27**, 5397–5430.
- Willis, B. T. M. (1973). *Chemical Applications of Thermal Neutron Scattering*, p. 250. Oxford University Press.